

1 Poroelastic effects destabilize mildly rate-strengthening friction to
2 generate stable slow slip pulses

3 Elías R. Heimisson^{a,*}, Eric M. Dunham^{a,b}, Martin Almqvist^a

4 ^a*Department of Geophysics, Stanford University, Stanford, California, USA*

5 ^b*Institute for Computational and Mathematical Engineering, Stanford University, Stanford, California,*
6 *USA*

7 **Abstract**

Slow slip events on tectonic faults, sliding instabilities that never accelerate to inertially limited ruptures or earthquakes, are one of the most enigmatic phenomena in frictional sliding. While observations of slow slip events continue to mount, a plausible mechanism that permits instability while simultaneously limiting slip speed remains elusive. Rate-and-state friction has been successful in describing most aspects of rock friction, faulting, and earthquakes; current explanations of slow slip events appeal to rate-weakening friction to induce instabilities, which are then stalled by additional stabilizing processes like dilatancy or a transition to rate-strengthening friction at high slip rates. However, the temperatures and/or clay-rich compositions at slow slip locations are almost ubiquitously associated with rate-strengthening friction. In this study, we propose a fundamentally different instability mechanism that may reconcile this contradiction, demonstrating how slow slip events can nucleate with mildly rate-strengthening friction. We identify two destabilizing mechanisms, both reducing frictional shear strength through reductions in effective normal stress, that counteract the stabilizing effects of rate-strengthening friction. The instability develops into slow slip pulses. We quantify parameter controls on pulse length, propagation speed, and other characteristics, and demonstrate broad consistency with observations of tectonic slow slip events as well as laboratory tribology experiments.

8 *Keywords:* rate-and-state friction, poroelasticity, slow slip mechanics, rate-strengthening
9 friction, slip pulses, hydrogels

10 **1. Introduction**

11 Frictional instabilities are intrinsically linked with shear fracturing and material failure[1].
12 Earthquakes are notable examples of such instabilities, featuring explosive, inertially limited
13 rupture growth on faults following gradual development of instability. Yet not all faults slip
14 in earthquakes; some slide steadily in response to tectonic loading. This diversity in sliding
15 behavior is well explained by rate-and-state friction, an experimentally based description
16 of how friction, f , evolves with sliding velocity (i.e., slip rate, V) and sliding history. It is
17 widely thought[2] that instabilities during sliding require rate-weakening friction, in which f
18 decreases with increasing V (following a transient rate-strengthening response that stabilizes
19 short-wavelength perturbations). Likewise, rate-strengthening friction is linked to aseismic
20 slip, which is thought to occur steadily in the absence of changes in loading.

21 Slow slip events are challenging to reconcile with this understanding. Slow slip occurs in
22 subduction zones and possibly at the base of some strike-slip faults and is one component of
23 a class of sliding events that includes low-frequency earthquakes, tectonic tremor, tsunami
24 earthquakes, some landslides, and even stick-slip cycles on ice streams[3, 4]. Slow slip is also
25 thought to play an important role in injection-induced seismicity and reservoir stimulation by
26 hydraulic fracturing[5, 6]. In addition, slow slip has been observed in friction experiments,
27 in particular experiments on hydrogels that report spontaneous nucleation of slip pulses
28 that propagate faster than the loading speed but much slower than elastic wave speeds
29 [7, 8, 9, 10, 11].

30 The challenge posed by slow slip events is to simultaneously explain their unstable nature
31 (i.e., why the interface does not slide steadily) and why they do not continue to grow into
32 ruptures. Current theories posit that slow slip events nucleate under rate-weakening friction,
33 just like earthquakes, but then stall for a variety of reasons. These include a transition from
34 rate-weakening to rate-strengthening friction with increasing V , stabilization by dilatancy,
35 and interaction with frictional heterogeneities[12, 13, 14, 15, 16]. However, these theories

*Corresponding author:

Email address: eliasrh@stanford.edu (Elías R. Heimisson)

36 are inconsistent with indications that slow slip occurs in regions with rate-strengthening
37 friction, based on temperature conditions and/or clay-rich compositions[17, 18, 19, 20].

38 In this paper, we show that slow slip arises naturally from instabilities with mildly rate-
39 strengthening friction. These instabilities arise from two distinct mechanisms, both involving
40 configurations where slip couples to changes in effective normal stress. The first mechanism
41 occurs during sliding between poroelastic solids, for which compression or dilation of material
42 causes changes in pore pressure that alter frictional strength on the sliding interface [21, 22,
43 23] The second mechanism arises during sliding at the interface between two dissimilar elastic
44 solids, a process that alters total normal stress on the interface and hence frictional strength
45 [24]. We focus primarily on the poroelastic mechanism, but point out a correspondence
46 between the undrained poroelastic problem and the elastic bimaterial problem (at least for
47 a linearized friction law). We identify and characterize the sliding instabilities through 1.)
48 linear stability analysis of perturbations about steady sliding, and 2.) numerical simulations
49 of nucleation and propagation of slip pulses with fully nonlinear rate-and-state friction. Both
50 the stability analysis and numerical simulations are done for linear poroelastic solids.

51 This paper has four main sections. In Section 2 we present the conceptual and mathemat-
52 ical model. In Section 3 we develop solutions and discuss results for linearized rate-and-state
53 friction on a slip surface in a poroelastic medium. Specifically, we derive a characteristic
54 equation that describes the stability of the slip surface to a Fourier mode perturbation. Sec-
55 tion 4 describes numerical simulations that account for fully nonlinear frictional response.
56 Finally, Section 5 discusses and interprets the results in the context of observations of slow
57 slip in nature and laboratory experiments; furthermore, we speculate on the manifestation
58 of the rate-strengthening instability in 3D with possible application to subduction zone slow
59 slip events and other geological phenomena.

60 **2. Model**

61 In this section we elaborate on the conceptual, mathematical, and physical foundations
62 of the model before presenting the linearized stability analysis and numerical simulations
63 that will follow.

2.1. Fault structure, poroelastic effects, and coupling to fault strength

The mechanical and physical properties of the fault core, a region of the fault zone of high strain where slip localizes (Fig. 1a-b), are important to understanding how slip nucleates and propagates on natural faults. Fault cores are in many ways, both mechanically and chemically, different from the surrounding damage zone and, beyond that, the intact host rock. The fault core is thin compared to many seismologically relevant length scales, having a thickness (w in Fig. 1b) ranging from a few centimeters to meters [25]. Fault cores in well-developed fault zones often have very low permeability [26, 27, 28] compared to the surrounding damage zone and host rock [29, 30]. It is worth noting that in the analysis of this paper, we will use the concept of a fault core to describe a thin layer, in which slip localizes, with different mechanical and hydrological properties than the surrounding medium. However, in non-geological applications, the fault core may be regarded as a tribofilm that is produced by long-term wear of the frictional interface.

In this study, we assume that slip has localized at the boundary of the fault core (Fig. 1a-b), a configuration that maximizes the potential for instability compared to other locations within the fault core, as shown subsequently. Field exposures of formerly active faults also often feature localization on one side of the core [31, 32, 33].

Spatially non-uniform slip in this configuration compresses material on one side of the interface and dilates it on the opposite side, altering fluid pressure through poroelastic coupling [21, 22, 23, 34, 35]. Furthermore, this process is asymmetric, with pore pressure increases on one end of a slipping zone matched by corresponding decreases in pore pressure on the opposite end. The relatively impermeable fault core prevents pressure equilibration by flow across the core. These changes in pressure cause changes in the effective normal stress on the slip surface that asymmetrically alter the shear strength of the fault [23, 34, 35]. Slip localization to the boundary of the core thus gives rise to an asymmetry that favors propagation in one direction, with the favorable direction determined by which boundary of the core hosts the slip surface. A related bimaterial effect altering normal stress occurs during sliding between elastically dissimilar solids [24, 36, 37, 38]. In the elastic bimaterial effect, directionality is determined by the material properties, and can not be altered by

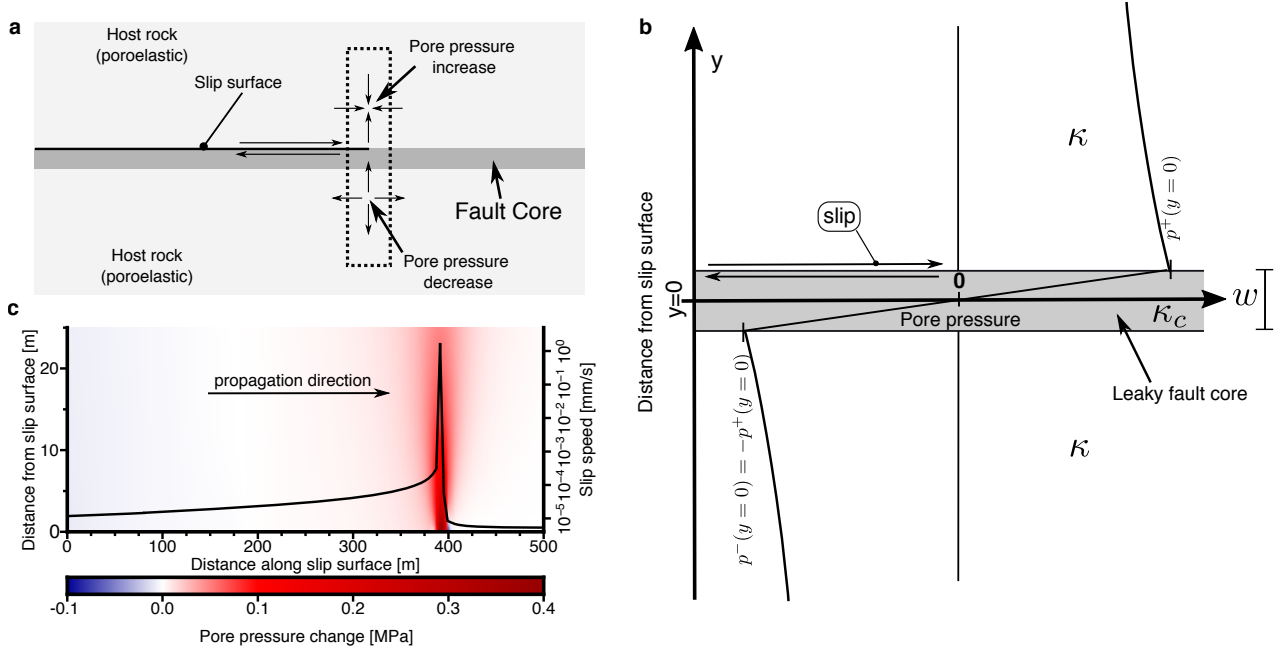


Figure 1: **a** Schematic of fault zone with slip localized on one side of the low permeability core, idealized in our study as having infinitesimal width with respect to the perturbation wavelength λ . Pressure changes are caused by compression/dilation of the near-fault material. **b** Zoomed-in view of dashed box in **a**, showing pore pressure change across sliding interface. For across fault diffusion we consider the core to have thickness $w \ll \lambda$ and mobility κ_c , which may be different from the surrounding host rock mobility κ . **c** Simulated slow slip pulse; elevated pore pressure around the slip front weakens the interface, facilitating propagation.

93 the place of slip localization unless additional poroelastic effects occur. The strong sense
 94 of directionality in both the poroelastic and elastic bimaterial problems is a characteristic
 95 property of slip pulses (Fig. 1c). Experiments confirm that slip instabilities on poroelastic
 96 and/or elastic bimaterial interfaces often develop into propagating slip pulses [9, 39].

97 In this study, we consider sliding on a slip surface at the edge of a fault core of width
 98 w with mobility (permeability divided by fluid viscosity) κ_c . The rock outside the fault
 99 core has a possibly different mobility κ . For simplicity, we do not distinguish between the
 100 damage zone and host rock in this study.

101 *2.2. Poroelasticity*

102 Here we describe the governing equations of quasi-static linear isotropic poroelasticity
 103 and the interface conditions that we impose in our problem. The displacements u_i and pres-
 104 sure changes p are governed by a set of four coupled partial differential equations. Assuming
 105 that body forces are negligible, these are

$$Gu_{i,kk} + \frac{G}{1-2\nu}u_{k,ki} = \alpha p_{,i} \quad (1)$$

106 and

$$\frac{1}{M}p_{,t} - \kappa p_{,kk} = -\alpha u_{k,kt}, \quad (2)$$

107 where summation over repeated indices is implied and subscript $,t$ denotes the partial time
 108 derivative and $,k$ denotes the partial spatial derivative in direction x_k . The material pa-
 109 rameters are the shear modulus G , drained Poisson ratio ν , Biot-Willis coefficient α , Biot
 110 modulus M , and mobility κ . In other sections, different sets of five parameters will be
 111 introduced if they provide simpler expressions. Specifically, we use Skempton's coefficient
 112 B , the undrained Poisson ratio ν_u , and the hydraulic diffusivity $c = \kappa M$. Note that B
 113 relates undrained response in pore pressure p perturbations to changes in mean stress:
 114 $p = -B\Delta\sigma_{kk}/3$ [22]. We may relate B and ν_u to the material parameters in Eqs. 1
 115 and 2 using the following equations:

$$B = \frac{3M\alpha(1-2\nu)}{2G(1+\nu) + 3M\alpha^2(1-2\nu)}, \quad (3)$$

$$\nu_u = \frac{2G\nu + M\alpha^2(1-2\nu)}{2G + 2M\alpha^2(1-2\nu)}; \quad (4)$$

116 furthermore, a relationship between B and ν_u is given by

$$B = \frac{3(\nu_u - \nu)}{\alpha(1-2\nu)(1+\nu_u)}. \quad (5)$$

117 In this study we seek a solution of Eqs. 1 and 2 for two half-spaces under the assumption
 118 of 2-D plane strain deformation, thus reducing the system to three coupled partial differential

119 equations. We utilize an x - y Cartesian coordinate system with $y = 0$ being the sliding
120 interface. Our first objective is to obtain linear relations between slip and stress and pressure
121 change on the interface, which are used in subsequent sections when enforcing a specific
122 interface friction law. To obtain these linear relations, the following boundary and interface
123 conditions are imposed:

$$\lim_{y \rightarrow 0^\pm} u_x^+ - u_x^- = \delta, \quad (6)$$

$$\lim_{y \rightarrow 0^\pm} u_y^+ - u_y^- = 0, \quad (7)$$

$$\lim_{y \rightarrow \pm\infty} u_i^\pm = 0, \quad (8)$$

$$\lim_{y \rightarrow \pm\infty} p^\pm = 0, \quad (9)$$

$$\lim_{y \rightarrow 0^\pm} \sigma_{xy}^+ - \sigma_{xy}^- = 0, \quad (10)$$

$$\lim_{y \rightarrow 0^\pm} \sigma_{yy}^+ - \sigma_{yy}^- = 0, \quad (11)$$

124 where superscripts $+$ or $-$ represent the upper ($y > 0$) or lower ($y < 0$) half-spaces. The first
125 equation imposes slip δ across the interface. The second equation assures that no opening
126 or interpenetration occurs on the interface. The third requires displacements and stresses to
127 vanish at infinity; the fourth requires pore pressure changes and fluid flux to also vanish at
128 infinity. The fifth and sixth equations enforce Newton's third law across the interface. Two
129 more conditions are required on the fault to fully specify the problem.

130 2.3. Leaky fault model

131 We next introduce two pressure and fluid flow interface conditions on the slip surface. We
132 assume that slip perturbations have wavelengths λ much larger than the fault core thickness
133 w (Figure 1b). This scale separation, together with symmetry (or antisymmetry) of fields
134 across the fault, permits application of an approximate leaky fault model recently introduced
135 by Song and Rudnicki[40]. The leaky fault model accounts for flow across the fault core via
136 linear relations between pore pressure and its gradient in the fault-normal direction on the

137 two sides of the slip surface:

$$\frac{dp^\pm}{dy} \Big|_{y=0^\pm} = \pm \frac{\kappa_c}{\kappa} \frac{2p^\pm}{w}. \quad (12)$$

138 We note that if $\kappa_c/\kappa \rightarrow 0$ then $dp^\pm/dy \rightarrow 0$ at $y = 0^\pm$, thus providing boundary conditions
 139 corresponding to an impermeable fault core. However, if $\kappa/\kappa_c \rightarrow 0$ then $p^\pm \rightarrow 0$, which
 140 corresponds to a fully permeable fault core.

141 2.4. Solution of poroelastic problem with imposed slip

142 The governing equations and interface conditions (with imposed slip) can be solved using
 143 a Fourier transform in fault-parallel distance x and Laplace transform in time t , defined as

$$\hat{\delta}(s, k) = \int_0^\infty \int_{-\infty}^\infty \delta(t, x) e^{-ikx-st} dx dt \quad (13)$$

144 for slip and similarly for other fields. The procedure in Appendix A provides linear relations
 145 between the transformed shear stress change on the interface, $\hat{\tau}$, pore pressure change on
 146 the two sides of the interface, \hat{p}^\pm , and slip, $\hat{\delta}$:

$$\hat{\tau} = -\frac{G|k|\hat{\delta}}{2(1-\nu_u)} H_1(s, k) \quad (14)$$

147 and

$$\hat{p}^\pm = \mp \frac{ikGB\hat{\delta}}{3} \frac{1+\nu_u}{1-\nu_u} H_2(s, k), \quad (15)$$

148 where

$$H_1(s, k) = 1 - \frac{2(\nu_u - \nu) ck^2}{1 - \nu} \frac{1 + \mathcal{F}}{s \mathcal{F} + \sqrt{1 + s/ck^2}} \left(\sqrt{1 + s/ck^2} - 1 \right), \quad (16)$$

149 and

$$H_2(s, k) = \frac{\sqrt{1 + s/ck^2} - 1}{\sqrt{1 + s/ck^2} + \mathcal{F}}, \quad (17)$$

150 in which \mathcal{F} is a nondimensional parameter (given a fixed k) that characterizes the importance
 151 of flux across the fault:

$$\mathcal{F} = \frac{\kappa_c}{\kappa} \frac{2}{|k|w}. \quad (18)$$

152 Note that both $H_1(s, k)$ and $H_2(s, k)$ go to unity in the limit where $ck^2/s \rightarrow 0$ assuming
 153 $\mathcal{F} < \infty$. We will refer to this as the undrained limit, where the change in effective normal

154 stress is the largest. We explore this limit later in detail due to mathematical simplicity and
 155 the physically interesting effects that arise from changes in the effective normal stress. If
 156 $\mathcal{F} \rightarrow \infty$, then $\hat{p}^\pm \rightarrow 0$, which corresponds to a fully permeable fault, in which case there is
 157 no change in effective normal stress on the fault. Note that $\kappa_c/\kappa = c_c M_c/cM$, and thus \mathcal{F}
 158 can be written in terms of the hydraulic diffusivities c and Biot moduli M of the host rock
 159 and fault core.

160 2.5. Rate-and-state friction

161 Frictional sliding on the slip surface is governed by rate-and-state friction, which provides
 162 a relation between shear strength τ , effective normal stress σ' , and friction coefficient f that
 163 depends on sliding velocity V and state variable Ψ . The latter obeys a state evolution
 164 equation.

165 In the first part of this study, we perform a linear stability analysis using a general form
 166 of linearized rate-and-state friction, valid for small perturbations about a steady sliding
 167 solution at slip speed V_0 , that encompasses a broad class of steady state friction and state
 168 solution laws[36]:

$$\frac{d\tau}{dt} = \frac{a\sigma'_0}{V_0} \frac{dV}{dt} + (f_0 - \alpha_{LD}) \frac{d\sigma'}{dt} - \frac{V_0}{L} \left[\tau - f_0\sigma' - \frac{(a-b)\sigma'_0}{V_0} (V - V_0) \right], \quad (19)$$

169 in which f_0 is the steady-state coefficient of friction at sliding velocity V_0 , α_{LD} is the Linker-
 170 Dieterich constant [41], σ'_0 is the initial effective normal stress, L is the state evolution
 171 distance, and a and b are dimensionless parameters that are related to the rate and state
 172 dependence of friction, respectively.

173 In the second part of this study, we perform simulations with nonlinear rate-and-state
 174 friction. For this we set $\alpha_{LD} = 0$ and use a standard logarithmic dependence of steady state
 175 friction coefficient on slip velocity together with the slip evolution law [e.g. 36]

$$f(V, \Psi) = a \operatorname{arcsinh} \left(\frac{V}{2V_0} e^{\Psi/a} \right), \quad (20)$$

$$\frac{\partial \Psi}{\partial t} = -\frac{V}{L} [f - f_{ss}(V)], \quad (21)$$

176 where σ' is the effective normal stress, the steady state friction coefficient is

$$f_{ss}(V) = f_0 + (a - b) \ln(V/V_0). \quad (22)$$

177 Friction is said to be rate-strengthening (under steady sliding conditions) if $a - b > 0$ and
 178 rate-weakening if $a - b < 0$. Linearization of Eqs. 20–22 yields Eq. 19.

179 2.6. Parameter values

180 For the analysis and simulations we present, we assume a set of reference parameters
 181 (Table 1), which are typical for many geological settings and problems. Unless otherwise
 182 explicitly stated they are kept constant throughout this study, but frequently we will vary
 183 one or more parameter systematically while maintaining the others as listed in Table 1.

184 3. Linear stability analysis

185 In this section we investigate the linear stability of steady state sliding at slip velocity V_0
 186 to small Fourier mode perturbations. We show that steady sliding with a low permeability
 187 fault core is conditionally unstable for mildly rate-strengthening friction, in the sense that
 188 that small amplitude perturbations can spontaneously grow to nucleate slip instabilities.
 189 Later we demonstrate how these instabilities evolve, under nonlinear friction effects, into
 190 propagating slow slip pulses.

191 3.1. Characteristic equation

192 Applying a Fourier transform in x and a Laplace transform in time, Eq. 19 is

$$\left(s + \frac{V_0}{L}\right) \hat{\tau} = \left[f_0 \left(s + \frac{V_0}{L}\right) - \alpha_{LD}s\right] \hat{\sigma}' + \left[\frac{a\sigma'_0}{V_0}s^2 + \frac{(a-b)\sigma'_0}{L}s\right] \hat{\delta}. \quad (23)$$

193 Next we insert the linear poroelastic relations, Eqs. 14 and 15, into Eq. 23 and obtain
 194 the characteristic equation. Assuming slip localization on the $y > 0$ side of the interface
 195 (Fig. 1b), such that $\hat{\sigma}' = -\hat{p}^+$, the characteristic equation is

Table 1: Reference parameters

Symbol	Description	Value
<i>Material properties</i>		
B	Skempton's coefficient	0.6
ν	Drained Poisson's ratio	0.25
ν_u	Undrained Poisson's ratio	0.35
G	Shear modulus	30 GPa
<i>Friction</i>		
L	Characteristic state evolution distance	10 μm
a	Rate dependence of friction	0.01
$a - b$	Degree of rate-strengthening	1.5×10^{-4}
α_{LD}	Linker-Dieterich constant [41]	0
V_0	Steady state sliding velocity	10^{-9} m/s
f_0	Steady state coefficient of friction at V_0	0.6
σ'_0	Initial effective normal stress	50 MPa
<i>Nondimensional parameters</i>		
γ	Lateral diffusion stabilization	0.08
ϵ	Across fault flow stabilization (Eq. 28)	0
<i>Physical scales — dependent on parameters above</i>		
λ_c	Approximate preferred wavelength (Eq. 25)	
v_p	Phase velocity of λ_c (Eq. 26)	
r	Growth rate of λ_c (Eq. 27)	

$$\frac{a\sigma'_0}{V_0}s^2 + \left[\frac{(a-b)\sigma'_0}{L} + \frac{G|k|H_1(s,k)}{2(1-\nu_u)} - ik\frac{BG}{3}\frac{1+\nu_u}{1-\nu_u}(f_0 - \alpha_{LD})H_2(s,k) \right] s + \frac{V_0}{L} \left[\frac{G|k|H_1(s,k)}{2(1-\nu_u)} - ik\frac{BG}{3}\frac{1+\nu_u}{1-\nu_u}f_0H_2(s,k) \right] = 0. \quad (24)$$

196 The undrained limit, which was previously described ($ck^2/s \rightarrow 0$ and $\mathcal{F} < \infty$), is attained
 197 from Eq. 24 by setting $H_1 = H_2 = 1$.

198 3.2. Undrained limit

199 In order to gain insight into the stability of the fault we solve Eq. 24 for $s(k)$ with
 200 near-rate-neutral friction, $a - b = O(10^{-4})$ (Fig. 2). The figure reveals that a range of
 201 wavelengths is linearly unstable to small perturbations at mildly rate-strengthening friction.
 202 Unlike instabilities at the interface of two identical elastic half-spaces, there is a wavelength
 203 of maximum growth rate, which we will refer to as the **preferred wavelength**, noting that
 204 both larger and smaller wavelengths are stable. The stability at large wavelengths suggests
 205 pulse-like propagation, rather crack-like expansion of slip instabilities. Further suggesting
 206 pulse-like behavior is the directional dependence of the solutions to Eq. 24, which assumes
 207 slip localization on $y > 0$ side of the fault core. The equation predicts that a perturbation
 208 with $k > 0$ (propagating to the right, as shown in Fig. 1c) experiences pore pressure changes
 209 that can overcome the otherwise stabilizing effects of mildly rate-strengthening friction, but
 210 perturbations with $k < 0$ (i.e., propagating to the left, not shown) have pressure changes
 211 that further stabilize sliding, due to the sign change in pore pressure (Eq. 15). This gives
 212 rise to directionality and determines the pulse propagation direction. For localization on
 213 the $y < 0$ side of the fault core, the characteristic equation is attained by changing the sign
 214 of the pore pressure terms (that is changing $-ik \rightarrow ik$ in Eq. 24). Then perturbations
 215 with $k < 0$ can be unstable under rate-strengthening friction, but $k > 0$ perturbations are
 216 always stable. This suggests that pulses may propagate in both directions on the same fault
 217 depending on where localization occurs. However, one direction may be favored if there are
 218 additional elastic bimaterial effects, as we discuss later.

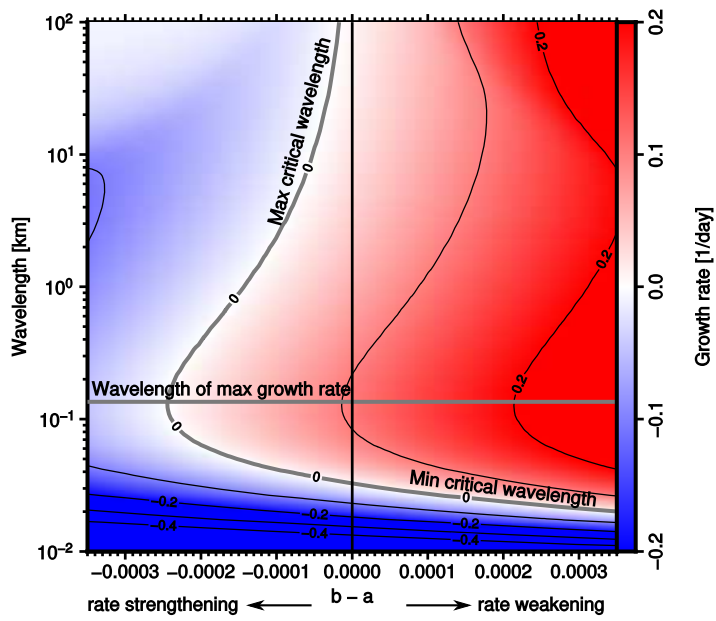


Figure 2: Growth/decay rate from linear stability analysis in the undrained limit, with the gray contour marking neutral stability. For rate-weakening friction ($b - a > 0$), all wavelengths greater than a critical wavelength are unstable. For rate-strengthening friction ($b - a < 0$), instability occurs for a range of wavelengths provided that $a - b$ is sufficiently small. The wavelength of maximum growth rate, also marked, is relatively independent of $a - b$. Parameters given in Table 1. See also Fig. 3.

219 For simplicity and insight, we provide approximate expressions valid in the undrained
 220 limit (negligible fluid flow) near rate-neutral friction ($a \sim b$) and assuming $\alpha_{LD} = 0$. We
 221 observed from numerical solutions to Eq. 24 that $|\text{Re}(s)| \ll |\text{Im}(s)|$ near rate-neutral fric-
 222 tion, meaning that the growth rate of perturbations is much smaller than their angular
 223 frequency. Given these observations we assume the second order $\text{Re}(s)^2$ term may be ig-
 224 nored which results in explicit closed form solutions for $\text{Re}(s)(k)$ and $\text{Im}(s)(k)$, valid if
 225 $\text{Re}(s)(k) \ll \text{Im}(s)(k)$. Then solving $d\text{Re}(s)(k)/dk = 0$ for k gives an approximate expres-
 226 sion for the preferred wavenumber. Substituting this approximate expression in $\text{Re}(s)(k)$ and
 227 $\text{Im}(s)(k)$ provides growth rate and angular frequency evaluated at the preferred wavenum-
 228 ber. However, in spite of the $|\text{Re}(s)(k)| \ll |\text{Im}(s)(k)|$ assumption, these expressions are too
 229 complicated to provide insight into first order effects. We perform a Taylor expansion to
 230 leading order in Bf_0 , recognizing that under most conditions Bf_0 is smaller than unity. This
 231 approximation of the preferred wavelength is

$$\lambda_c \equiv \frac{9\pi LG}{\sigma'_0 a(1 + \nu_u)^2(1 - \nu_u)(Bf_0)^2}. \quad (25)$$

232 Slip pulses propagate along the interface in the direction of strength reduction (Fig. 1c),
 233 and we gain insight into their propagation speed by deriving the approximate phase velocity,
 234 $v_p = -\text{Im}(s)/k$, at λ_c :

$$v_p \equiv \frac{3V_0 G}{2\sigma'_0 a(1 + \nu_u)(1 - \nu_u)Bf_0}. \quad (26)$$

235 The approximate growth rate of λ_c is

$$r \equiv \frac{V_0}{L} \left[\frac{(Bf_0)^2}{18} (\nu_u + 1)^2 + \frac{b - a}{2a} \right]. \quad (27)$$

236 Equation 27 also quantifies the maximum rate-strengthening $a - b$ that can be destabilized
 237 by effective normal stress changes: $(a - b)_{\text{crit}} \approx a(1 + \nu_u)^2(Bf_0)^2/9$.

238 3.3. Correspondence between undrained poroelastic and elastic bimaterial problems

239 The linear stability results for the elastic bimaterial problem[36, 38] are mathematically
 240 identical to those describing the undrained poroelastic problem, with the substitution $G/(1 -$
 241 $\nu_u) \rightarrow M$ and $2B(1 + \nu_u)/3 \rightarrow \beta$, where M and β are elastic bimaterial parameters defined

242 by Rice et al.[36] to quantify elastic moduli and material contrast, respectively. Apparently,
 243 though, the connection between slow slip pulses and stability characteristics was overlooked
 244 in previous studies.

245 Note that for natural faults, β is typically less than 0.1 [36], while $B \approx 0.5$ to 0.9 [42].
 246 Thus we conclude that destabilization by poroelastic effects is more likely to cause slow slip
 247 instabilities than elastic bimaterial effects on rate-strengthening faults, justifying our focus
 248 on the poroelastic instability numerical simulations.

249 *3.4. Stabilizing effects of diffusion and fluid flow*

250 Both lateral diffusion and diffusion across the fault core will act to equilibrate poroelastic
 251 pressure changes. If this equilibration process occurs sufficiently fast, as compared to the
 252 growth time of the instability described in previous sections, then sliding will be stabilized.
 253 Here we identify two nondimensional parameters, γ and ϵ , that quantify the importance of
 254 lateral and across-fault diffusion, respectively.

255 To determine the time scales over which pressure equilibration occurs, we examine Eq.
 256 17 that expresses pore pressure change on the fault. Pressure change vanishes if the function
 257 $H_2(s, k) \rightarrow 0$. This can occur if either ck^2/s (comparing Laplace parameter s to the diffu-
 258 sion time along the fault, $(k^2c)^{-1}$) or \mathcal{F} (quantifying across-fault pressure equilibration) is
 259 sufficiently large. Eq. 17 also reveals that the relative magnitude of ck^2/s and \mathcal{F} determines
 260 which equilibration mechanism is dominant. If $\mathcal{F}/\sqrt{1+s/ck^2} \ll 1$, then the fault core
 261 can be regarded as impermeable, so pressure equilibration occurs by lateral flow parallel to
 262 the fault. This will stabilize the system if ck^2/s is sufficiently large. We thus deduce that
 263 instability requires that both $\mathcal{F}/\sqrt{1+s/ck^2} \ll 1$ and $ck^2/s \ll 1$. However, $s = s(k)$ is
 264 generally complex and therefore inappropriate for use in defining dimensionless parameters.

265 We, therefore, nondimensionalize s and k , first by generic time and length scales, then
 266 later by selecting these scales as those characterizing the maximum growth rate instability
 267 under undrained conditions. Let s^* and k^* be characteristic growth rate and wavenumber,
 268 respectively, such that in a relevant range the nondimensional growth rate $\tilde{s} = s/s^*$ and
 269 wavenumber $\tilde{k} = k/k^*$ are both of order unity. It follows that $ck^2/s = c(k^*)^2/s^* \times \tilde{k}^2/\tilde{s}$,

270 where \tilde{k}^2/\tilde{s} is of order unity. The nondimensional parameter is identified as $\gamma \equiv c(k^*)^2/s^*$,
 271 which is the ratio the time scale of lateral diffusion, $[(k^*)^2c]^{-1}$ and the time scale of the
 272 instability $(s^*)^{-1}$. Instability is promoted by small values of γ .

273 Across-fault diffusion is negligible relative to lateral diffusion when $\mathcal{F}/\sqrt{1+s/ck^2} \ll 1$.
 274 To quantify the relative importance of these processes, we write $\mathcal{F} = 2\kappa_c/(\tilde{k}\kappa wk^*)$, from
 275 which we identify $\psi \equiv 2\kappa_c/\kappa wk^*$. Now $\sqrt{1+s/ck^2} \sim \sqrt{1+1/\gamma}$ and if $\gamma \ll 1$, as required
 276 for instability, then $\sqrt{1+1/\gamma} \approx \sqrt{1/\gamma}$. We then identify the nondimensional ratio that
 277 characterizes the competition between across-fault and lateral diffusion:

$$\epsilon \equiv \psi\sqrt{\gamma} = \frac{2\kappa_c}{\sqrt{\kappa w}} \sqrt{\frac{M}{s^*}}. \quad (28)$$

278 Instability is promoted by small values of ϵ .

279 Next we take $s^* = r$ in Eq. 27, with $a = b$ (rate-neutral friction), and $k^* = 2\pi/\lambda_c$ from
 280 Eq. 25. These scales are used to nondimensionalize results in Fig. 3. Fig. 3a and b show
 281 how stability at rate-neutral friction changes by systematically varying γ and ϵ , respectively,
 282 and solving Eq. 24 for $s = s(k)$. This comparison reveals that the choice of characteristic
 283 scales and nondimensional parameters is appropriate and the conditions $\epsilon, \gamma \ll 1$ yield the
 284 undrained response.

285 If $\epsilon \ll 1$, then the dominant diffusion mechanism is lateral and the fault core is effectively
 286 impermeable on relevant time scales, a necessary but not sufficient condition for instability.
 287 It is furthermore necessary that γ be sufficiently small such that lateral diffusion cannot
 288 stabilize the nucleation process. Interestingly, the condition on γ is far less restrictive than
 289 $\gamma \ll 1$, as Fig. 3a shows instability even for γ several orders of magnitude larger than unity.

290 In addition, Fig. 3c compares the approximate solutions of Eqs. 25, 26, and 27, developed
 291 under the assumption that $Bf_0 \ll 1$, with numerical solutions to Eq. 24, showing good
 292 agreement even though $Bf_0 = 0.36$. There is a clear peak in growth rate ($\text{Re}(\tilde{s})$) in the
 293 vicinity of the preferred wavelength for both rate-strengthening and rate-weakening friction.
 294 However, at increasingly rate-weakening friction a more rapidly growing instability occurs
 295 at smaller wavelengths.

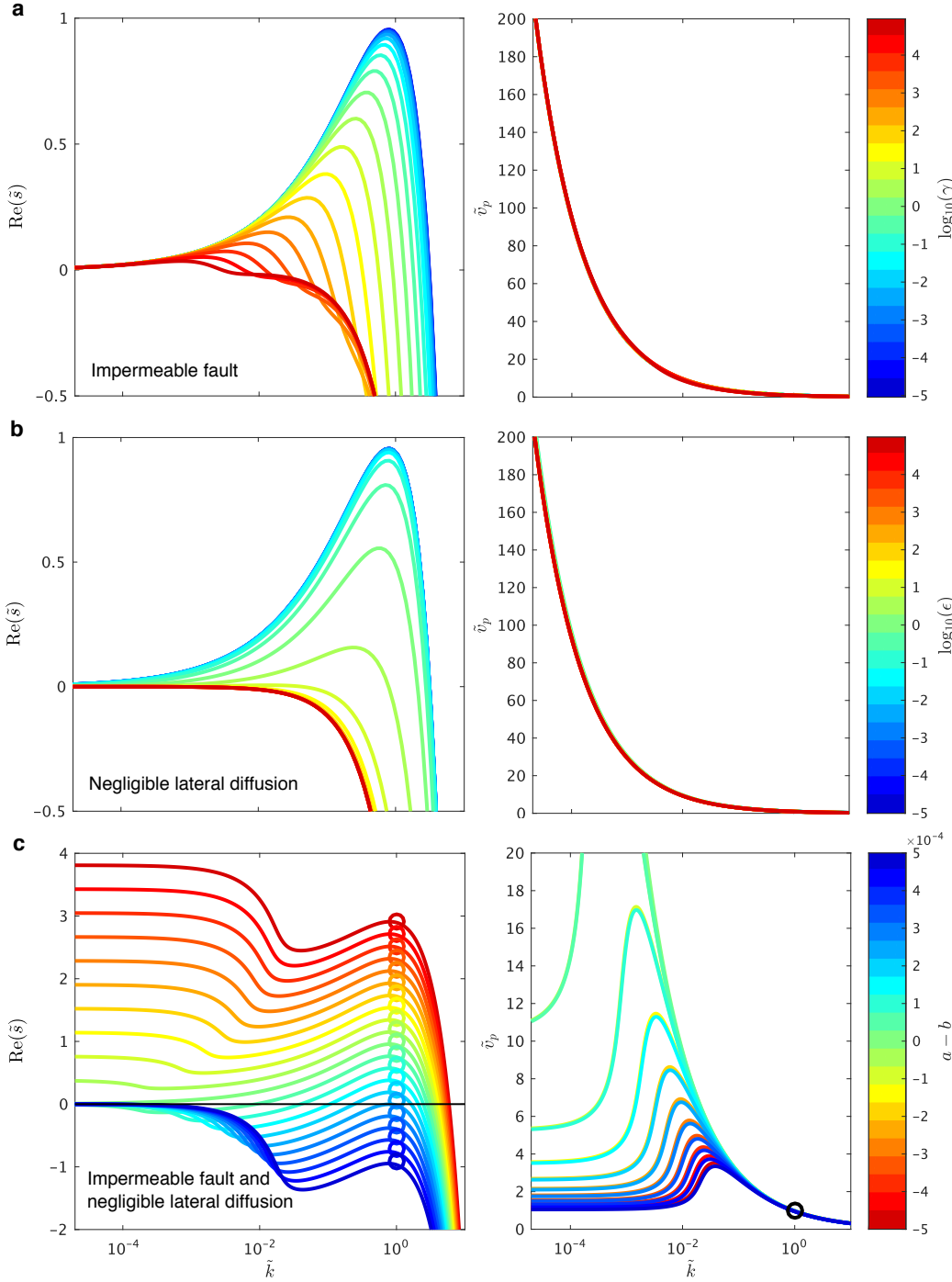


Figure 3: Linear stability analysis results showing nondimensional growth rate $\text{Re}(\tilde{s})$ and phase velocity \tilde{v}_p . **a**, Fault core is impermeable ($\psi = 0$, and thus $\epsilon = 0$) but lateral diffusion is allowed by changing γ . Friction is rate-neutral ($a = b$). Phase velocity is largely independent of γ . **b**, Negligible lateral diffusion ($\gamma = 2.4 \times 10^{-6}$), but ϵ is varied to explore effects of across-fault flow. Friction is rate-neutral. **c**, Effectively undrained limit ($\gamma = 2.4 \times 10^{-6}$, $\epsilon = 0$) for various $a - b$. Circles indicate approximate values given by Eqs. 25, 26, and 27. Phase velocity depends on $a - b$, although near the preferred wavelength it is relatively constant. Different values of γ and ϵ are explored by altering the mobility parameters κ and κ_c , respectively; other parameters are as listed in Table 1.

296 4. Numerical simulations

297 In the previous section we presented a linearized analysis that is only strictly valid for
298 small perturbations around steady state. Now we explore numerically how instabilities
299 evolve once nonlinear effects become important.

300 4.1. Problem statement and numerical methodology

301 The linear poroelastic equations are solved using a finite difference method with summation-
302 by-parts properties [43, 44]. Boundary conditions are enforced weakly using carefully chosen
303 penalty terms [45] such that numerical stability can be established using the energy method.
304 The numerical strategy follows [46] closely, using their fluid content formulation, but has
305 been extended to allow for stretched grids and enforce displacement boundary conditions
306 without approximating them by Robin conditions.

307 Simulations are conducted with a uniform grid spacing and periodic boundary conditions
308 in the x direction. The sliding interface ($y = 0$) is assumed to be impermeable ($\partial p/\partial y = 0$).
309 Assuming antisymmetry of displacement component u_x and symmetry of u_y about $y = 0$,
310 together with no opening or interpenetration of material across the interface, there is no
311 change in total normal stress σ_{yy} on the interface. We exploit these symmetries to model only
312 the top poroelastic block, replacing interface conditions with boundary conditions. The third
313 condition on the interface sets shear traction equal to the rate-and-state frictional strength.
314 The top boundary, parallel to the sliding interface, is placed at $y = 7\lambda_c$. Boundary conditions
315 on it are displacement at constant rate ($u_x = V_0 t/2$), no normal displacement ($u_y = 0$), and
316 no fluid flow through the boundary ($\partial p/\partial y = 0$). Results are relatively independent of the
317 latter two conditions if the domain is sufficiently large. For computational efficiency, we
318 applied a coordinate transformation in the y direction such that the grid spacing is finer
319 near the fault and becomes ten times larger over a distance of $1.5\lambda_c$. The domain size in
320 the x direction ranges from 17 to 50 times λ_c . Unless stated otherwise, we keep $\gamma = 0.08$
321 by varying the hydraulic diffusivity c , which ranges from 5×10^{-5} to $0.02 \text{ m}^2/\text{s}$. In the
322 simulations we only explore the limit of a fully impermeable fault ($\epsilon = 0$).

323 *4.2. Spontaneous formation of slip pulses*

324 Simulations with fully nonlinear rate-and-state friction response at mildly rate-strengthening
325 friction support the interpretations of the linear stability analysis. Linear stability at larger
326 wavelengths leads to slip pulses (Figs. 1c, 4, 5). Furthermore, we find that from slight
327 white noise perturbations to a fault driven at steady state, there is selection of a wavelength
328 of maximum growth rate which propagates along the fault with phase velocity; both the
329 wavelength and phase velocity are in agreement with linear theory (Fig. 4).

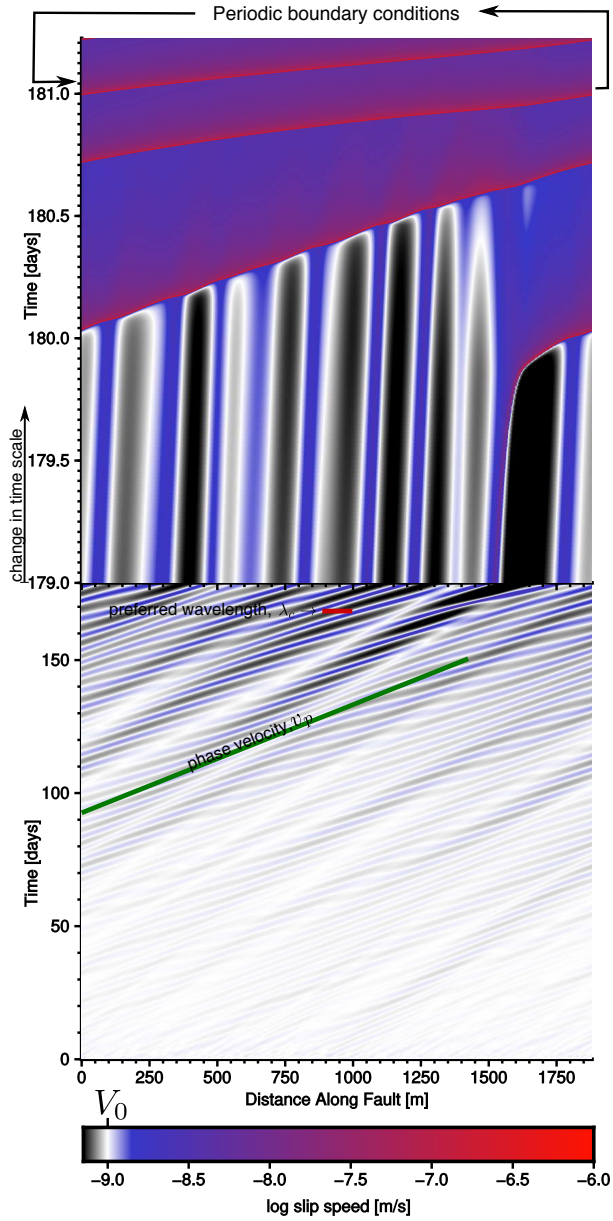


Figure 4: Evolution of slip rate in a simulation of sliding between poroelastic blocks with rate-strengthening friction. Certain wavelength perturbations, seeded from random initial conditions, grow in accordance with the linearized analysis until nonlinearities trigger slip pulse formation around 179-180 d (note change in time axis at 179 d). Continued propagation of the slip pulse smooths heterogeneities, and the system enters a steady, inhomogeneous sliding state with one active slip pulse (see also Fig. 1c). The approximate preferred wavelength λ_c (Eq. 25) and associated phase velocity v_p (Eq.26) from the linearized analysis are shown with red and green lines, respectively. Parameters given in Table 1.

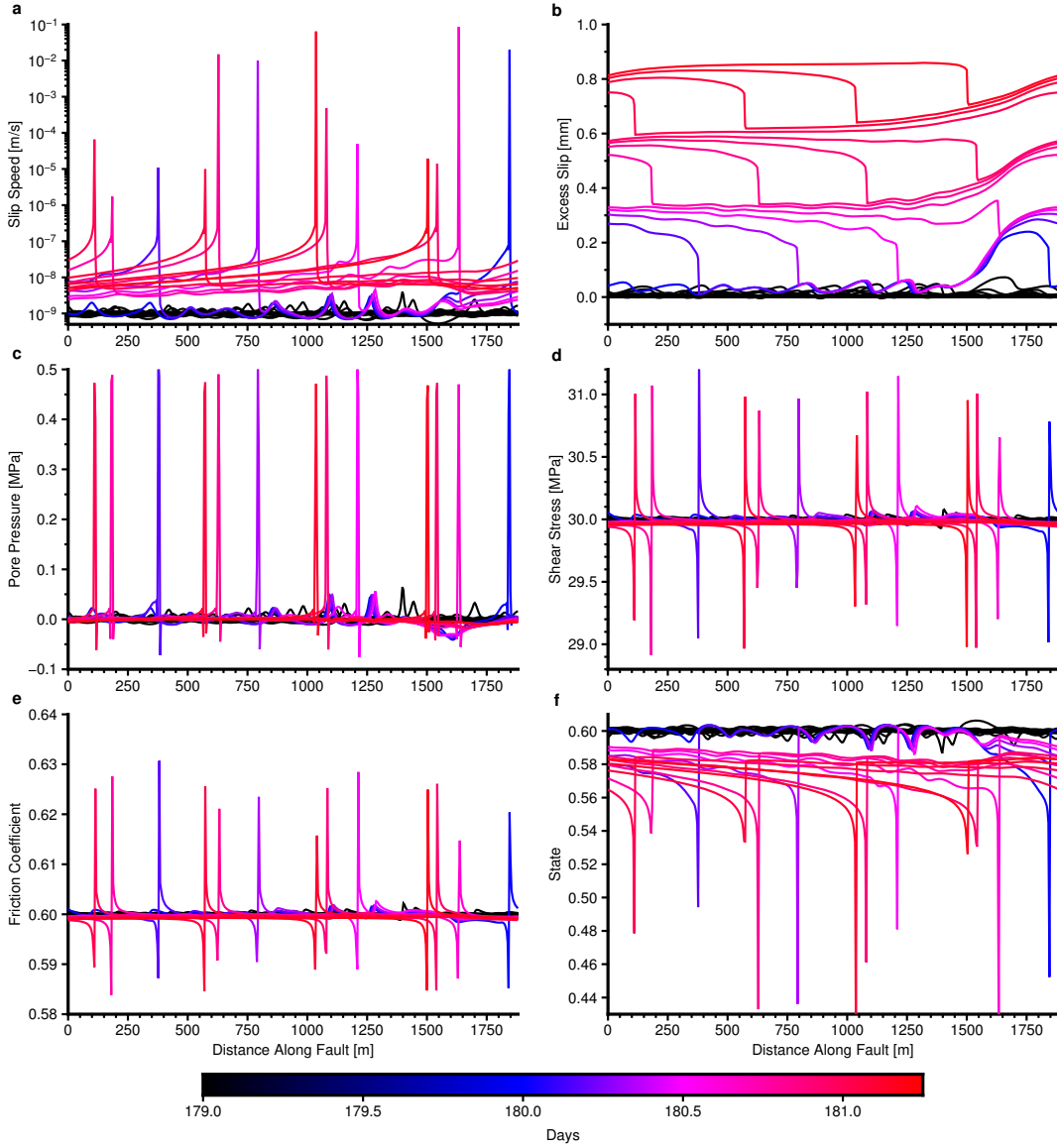


Figure 5: Snapshots of various fields on the sliding interface from the numerical simulation shown in Fig. 4. Lines that correspond to earlier times than day 179 (roughly the onset of the slip pulse) are black.

330 From investigating snapshots of various fields on the slip surface in the simulation in Fig.
 331 4 we observe several important characteristics of the slip pulses. Firstly, that the pulse slip
 332 in excess of steady state sliding is only about 0.3 mm (Fig. 5b). Secondly, the stress drop
 333 is only a fraction of a mega pascal. These are commonly observed characteristics of slow
 334 slip[47], which distinguish slow slip in nature from earthquakes. However these potential

335 observables depend on the assumed parameters, this dependence is explored in Fig. 6.

336 *4.3. Slip pulse characteristics*

337 Results from analysis of the linearized problem help explain parameter controls on pulse
338 length Λ_c and propagation speed V_p in the fully nonlinear simulations, though we find that
339 for the chosen parameters, slip pulses are 10 to 100 times longer and faster than predicted by
340 the linear theory. We quantify the characteristics of slip pulses in our numerical simulations
341 (Fig. 6) as follows. The simulation domain is $50\lambda_c$ in x and $7\lambda_c$ in y . A region along the
342 fault of length $3.5\lambda_c$ is perturbed about steady sliding to trigger instability. A slip pulse
343 forms and propagates into the unperturbed region, and its length Λ_c and propagation speed
344 V_p are measured. An example of this type of simulation is shown in Fig. 7. We define Λ_c
345 as the distance from the peak slip rate to where the slip rate has decayed to $1.5V_0$. The
346 cumulative excess slip is measured as the maximum average slip over the whole simulation
347 domain in excess of the background sliding. Similarly, the stress drop is measured as the
348 maximum spatially averaged shear stress drop during the simulation relative to the steady
349 state stress. Some variability in slip pulse characteristics is observed when changing how the
350 fault is initially perturbed or altering the domain size (which can affect how many pulses
351 nucleate and are simultaneously active). However, this variability is relatively minor, and
352 the approach outlined here gives consistent results that can be compared in a meaningful
353 manner.

354 Generally speaking, we find that the expressions for preferred wavelength and associated
355 phase velocity from the linearized analysis correctly predict parameter combinations that
356 determine slip pulse length and propagation speed. Furthermore, we see that stress drop
357 and excess slip depend on assumed parameters (Fig. 6c and d). For example, larger L will
358 result in larger excess slip and higher σ'_0 , which also means that in the simulation τ_0 is larger,
359 resulting in a higher stress drop.

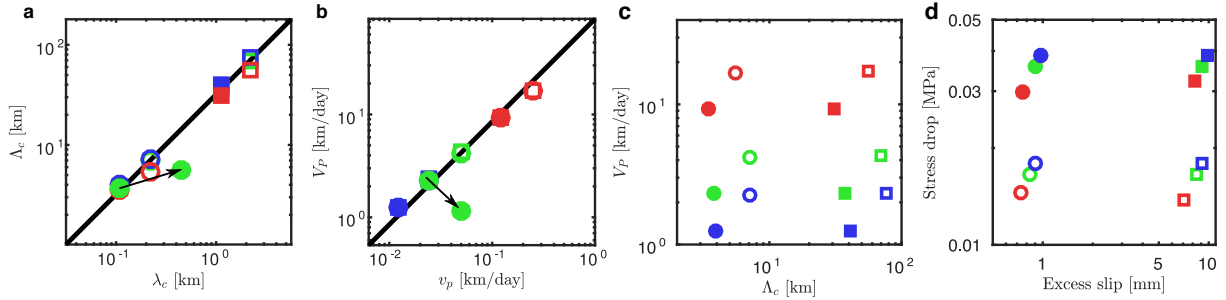


Figure 6: Comparison of simulated slip pulse characteristics with linear theory and observations. **a** Slip pulse length Λ_c is proportional to the preferred wavelength λ_c from the linear theory (Eq. 25), with approximate relationship $\Lambda_c \approx 32\lambda_c$ (black line). **b** Slip pulse propagation speed V_p is proportional to phase velocity of the preferred wavelength from the linear theory (Eq. 26), with approximate relationship $V_p \approx 85v_p$ (black line). **c** Cross-plot of slip pulse length and propagation speed. **d** Same as **c** for stress drop and slip. In all panels, symbols/colors indicate parameter variations: Circles, $L = 10 \mu\text{m}$; squares $L = 100 \mu\text{m}$. Filled symbols, $\sigma'_0 = 50 \text{ MPa}$; open symbols, $\sigma'_0 = 25 \text{ MPa}$. Blue, $V_0 = 5 \times 10^{-7} \text{ mm/s}$; green, $V_0 = 10^{-6} \text{ mm/s}$; red, $V_0 = 5 \times 10^{-6} \text{ mm/s}$. Arrow shows how changing $Bf_0 = 0.36$ to 0.18 for one simulation alters the scaling between linear and nonlinear characteristics, suggesting more complex dependence on Bf_0 than predicted by linear theory. Other parameters given in Table 1.

360 5. Discussion

361 5.1. Mildly rate-weakening friction

362 In Figs. 2 and 3c we observe at mildly rate-weakening friction that very large wavelengths
363 become unstable. These unstable wavelengths are relatively independent of poroelastic
364 processes and will remain unstable even if γ or ϵ are large. These wavelengths will, therefore,
365 likely cause seismic or inertially limited events, assuming that the fault is sufficiently large
366 to host such wavelengths. However, it is not clear at mildly rate-weakening friction if
367 all wavelengths will generate seismic events or manifest as slow slip pulses. Preliminary
368 nonlinear simulations under slightly rate-weakening friction (not shown here) suggest that
369 mildly rate-weakening friction also produces stable slow slip pulses. These simulations, done
370 with periodic boundary conditions, may simply not have a large enough domain to activate
371 wavelengths capable of producing seismic events. Indeed, even though the friction is rate-
372 weakening the stabilizing direct effect could prevent the instability from becoming seismic.

373 We suggest that a fruitful topic of future research may focus on investigating the partition
374 of wavelengths capable of producing seismic events or slow slip. This could shed light on
375 the potential transition from slow slip to seismic events.

376 *5.2. Experiments on hydrogels*

377 Perhaps the most convincing evidence for our theorized instability comes from labora-
378 tory hydrogel experiments[8, 7, 9, 10, 11]. A poroelastic gel block is slid across a glass
379 substrate, activating poroelastic and elastic bimaterial destabilizing effects. Consistent with
380 our predictions, steady sliding transitions spontaneously into slip pulses that advance, in
381 the direction of motion of the gel block, at speeds much slower than wave speeds but sev-
382 eral orders of magnitude faster than the driving speed V_0 . In particular, experiments in
383 an annular geometry[7], somewhat like our simulations with periodic boundary conditions,
384 show evolution to a steady, inhomogeneous sliding state (Fig. 7)) with direct proportionality
385 between pulse speed and V_0 (c.f., Eq. 26). Moreover, the pulse length is independent of V_0
386 (c.f., Eq. 25).

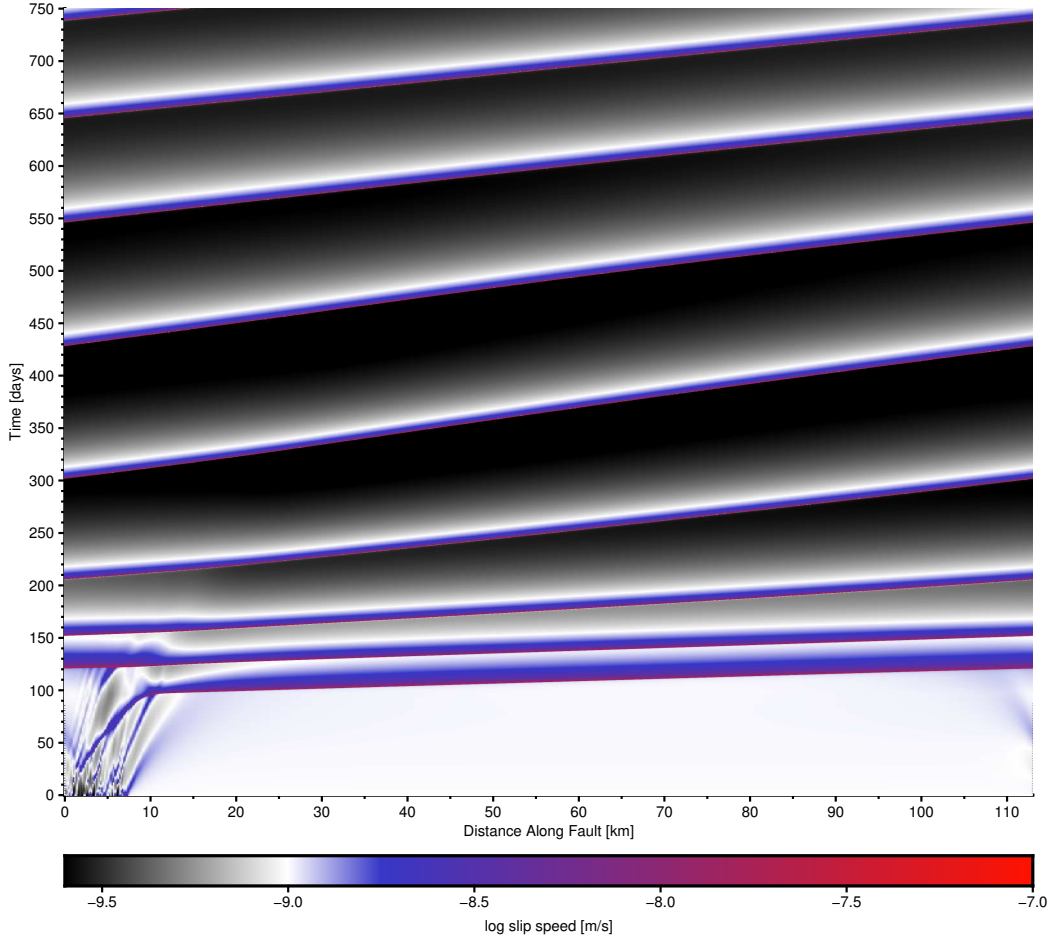


Figure 7: Evolution of slip rate in a simulation, similar to that shown in Figs. 4 and 5, but started from spatially localized perturbations in state ($0 < x < 3.5\lambda_c$). The simulation is run for longer, until the system evolves to steady, inhomogeneous sliding with one (or more) active slip pulses. This is an example of a simulation that is used to characterize slip pulse characteristics reported in Fig. 6. Parameters here correspond to open green square in Fig. 6.

387 5.3. Potential application to subduction zone slow slip

388 We propose that our mechanism could be applied to subduction zone slow slip. However,
 389 any true 3-D manifestations of this mechanism are hypothetical at this point and require
 390 further study. Direct application of our 2-D simulations to subduction zones is complicated
 391 by the 3-D nature of subduction slow slip, where slower migration along strike (i.e., in
 392 the invariant dimension in our simulations) is interspersed with faster along-dip transients

393 [48, 49]. Our instability mechanism would act only in the along-dip (mode II) direction,
 394 but along-strike (mode III) migration might be driven by stress transfer from currently
 395 slipping sections of the interface that activates instability in adjacent sections (Fig. 8).
 396 Furthermore, instabilities might also arise behind the main slip front and are predicted to
 397 propagate along-dip at higher velocities due to the accelerated sliding rate (c.f., Eq. 26).
 398 Similar ideas have been previously proposed based on tremor observations and geodetic
 399 modeling that suggest the large scale slow slip is, in reality, the manifestation of many slow
 400 transients[50]. It is worth noting that tremors migrate both up and down dip in subduction
 401 zones[49]. The poroelastic mechanism can explain both directions since the directionality
 402 is simply determined by in which side of the fault core slip localization occurs. However, a
 403 bimaterial destabilizing mechanism cannot explain migration in both directions.

404 The migration of tremor along the dip direction in subduction zones has been inferred to
 405 be faster than in simulations in the paper (Fig. 6). For example, in Japan they are around
 406 25 to 250 km/h compared to the along-strike migration of ~ 10 km/d [51]. Similar migration
 407 speeds of low frequency tremor are also observed on strike slip faults in the in-plane direction
 408 of sliding[52].

409 The mechanism we have presented can potentially explain the along-dip migration rates
 410 as large as observed in Japan and elsewhere if effective normal stress is sufficiently low.
 411 Indeed, previous authors have suggested that the effective normal stress may be around 0.1
 412 MPa[53]. The effective normal stress in most simulations in this study has been ~ 50 MPa,
 413 which results in propagation speed of about ~ 0.1 km/h. This is ~ 100 to 1000 times slower
 414 than the previously mentioned values for Japan. To test if comparable propagation speeds
 415 are observed in simulations at low effective normal stress, we ran two additional simulations
 416 at $\sigma'_0 = 1$ MPa and 0.1 MPa, but otherwise with reference parameters in Table 1. The
 417 setup of these simulations is otherwise the same as in Section 4.3. The low effective stress
 418 simulations reveal $V_P = 800$ km/d = 33 km/h for $\sigma'_0 = 0.1$ MPa and $V_P = 140$ km/d
 419 = 5.8 km/h for $\sigma'_0 = 1$ MPa. This demonstrates that at low effective normal stress the
 420 simulations predict the right order of magnitude for the tremor migration speeds observed
 421 in nature. Furthermore, the simulations at low effective normal stress show that the inferred

422 relationship $V_p \approx 85v_p$ in Fig. 6 still holds reasonably well.

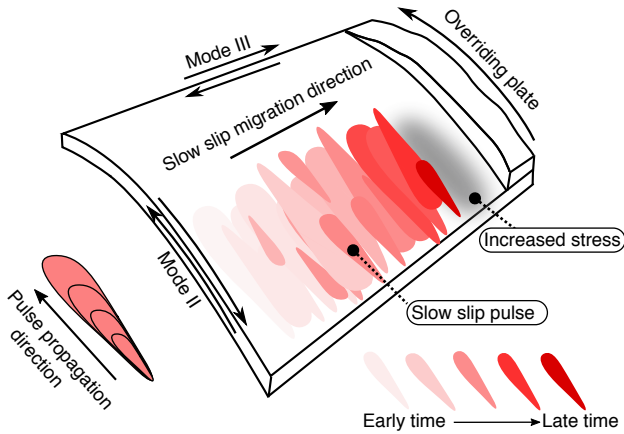


Figure 8: Schematic illustrating slip pulse instability in mode II direction, with mode III propagation driven by stress transfer.

423 5.4. Further applicability

424 Our results might also apply to other problems. These include magnitude 7 slow slip
 425 events of the Whillans Ice Plain[54], an Antarctic ice stream sliding on rate-neutral glacial
 426 till[55], and slow, episodic advance of landslide masses[56]. Finally, in the context of reser-
 427 voir geomechanics, if fault/fracture networks have heterogeneous frictional properties, the
 428 advance of slow slip along a rate-strengthening fault might manifest as a swarm of small
 429 earthquakes that migrates at relatively constant speed. Microseismic swarms accompanying
 430 fluid injection (e.g., in oil/gas operations) can indeed migrate faster than can be explained
 431 by pore pressure diffusion, possibly as a consequence of aseismic slip[6]. Additionally, the
 432 possibility of slow slip with rate-strengthening friction brings more consistency to the hypoth-
 433 esized role of slow slip in reservoir stimulation (permeability enhancement by fluid injection
 434 and hydraulic fracturing)[5]. Reservoir rocks such as shales contain clays and organics that
 435 are experimentally linked to rate-strengthening behavior[17]. The reservoir setting might
 436 also be ideal for model validation through direct measurements of pore pressure changes on
 437 or adjacent to faults concurrently with slip using recently developed borehole instruments[6].

438 **6. Conclusions**

439 We have investigated spontaneously occurring sliding instabilities that occur with mildly
440 rate-strengthening friction due to the coupling of slip and effective normal stress via two
441 different mechanism. This type of instability is fundamentally different from standard
442 earthquake-inducing instabilities with rate-weakening friction in that they are characterized
443 by a preferred wavelength having a maximum growth rate, with stability at both smaller
444 and larger wavelengths, and a strong preference in propagation direction. Simulations with
445 nonlinear rate-and-state friction show that these instabilities become slow slip pulses and
446 are broadly consistent with many aspects of slow slip in nature, such as low stress drops
447 and small slip distances. Furthermore, we find quantitatively similar propagation speeds of
448 pulses as compared to tectonic tremor and geodetically inferred slow slip migration speeds
449 under low effective normal stress conditions. We also observe qualitative consistency with
450 slow slip pulses identified in experiments on hydrogels. We have proposed a conceptual
451 model for how this type of instability might manifest in 3-D in a subduction zone setting,
452 where unstable pulses propagate in the along-dip (mode II) direction and along-strike (mode
453 III) migration is driven by secondary stress transfer due to cascading of pulses. However, we
454 recognize that in order to make a full comparison to slow slip in experiments and geological
455 settings we need to understand how the reported frictional instabilities manifest in three di-
456 mensions. In summary, our work demonstrates how poroelastic and elastic bimaterial effects
457 can destabilize mildly rate-strengthening sliding to generate slow slip events having features
458 consistent with observations.

459 **Appendix A. Poroelastic solution**

460 This appendix outlines the derivation of the linear relations between shear stress change
461 and slip and pore pressure change and slip that are implemented in deriving the characteristic
462 equation 24.

463 We solve Eqs. 1 and 2 using the method of displacement functions[57, 58], which are a
464 special case of the Biot potentials[59] applicable to plane strain problems. In order to find

465 the displacement functions, \mathcal{S} and \mathcal{E} , we solve

$$\nabla^2 \mathcal{S} = 0, \quad (\text{A.1})$$

$$\frac{\partial}{\partial t}(\nabla^2 \mathcal{E}) - c\nabla^4 \mathcal{E} = 0. \quad (\text{A.2})$$

466 By Fourier transforming with respect to x , with wavenumber k , and Laplace transforming
 467 in time, with Laplace parameter s , the problem is reduced to ordinary differential equations
 468 in y . Transformed fields are denoted as \hat{p} for p , etc. The transformed equations can be
 469 solved analytically. Disregarding the solution terms that diverge at infinity, we find

$$\hat{\mathcal{E}}^\pm = C_1^\pm \exp(\pm |k|y) + C_2^\pm \exp(\pm \sqrt{k^2 + s/cy}), \quad (\text{A.3})$$

$$\hat{\mathcal{S}}^\pm = C_3^\pm \exp(\pm |k|y), \quad (\text{A.4})$$

470 where C_1^\pm , C_2^\pm , and C_3^\pm are determined by interface conditions. Transforming the displace-
 471 ments functions into physical fields give the displacements and pore pressure as [42]

$$\hat{u}_x^\pm = -ik\hat{\mathcal{E}}^\pm + ik y \hat{\mathcal{S}}^\pm, \quad (\text{A.5})$$

$$\hat{u}_y^\pm = -\frac{\partial \hat{\mathcal{E}}^\pm}{\partial y} + y \frac{\partial \hat{\mathcal{S}}^\pm}{\partial y} - (3 - 4\nu_u) \hat{\mathcal{S}}^\pm, \quad (\text{A.6})$$

$$\hat{p}^\pm = -G \frac{2(1 - \nu)}{\alpha(1 - 2\nu)} \left[-k^2 \hat{\mathcal{E}}^\pm + \frac{\partial^2 \hat{\mathcal{E}}^\pm}{\partial y^2} - \frac{2(\nu_u - \nu)}{1 - \nu} \frac{\partial \hat{\mathcal{S}}^\pm}{\partial y} \right]. \quad (\text{A.7})$$

472 The stresses σ_{ij} are obtained from Hooke's law,

$$\sigma_{ij} = 2G\epsilon_{ij} + \frac{2G\nu}{1 - 2\nu} \epsilon_{kk} \delta_{ij} - \alpha p \delta_{ij}, \quad (\text{A.8})$$

473 where δ_{ij} is the Kronecker delta and ϵ_{ij} is the strain tensor, relevant transformed components
 474 of which are written as $\hat{\epsilon}_{xx}^\pm = ik\hat{u}_x^\pm$ and $\hat{\epsilon}_{xy}^\pm = (ik\hat{u}_y^\pm + \hat{u}_{x,y}^\pm)/2$, for example.

475 The C_1^\pm , C_2^\pm , and C_3^\pm are then determined using a symbolic manipulator where the
 476 appropriate boundary conditions are matched (Sections 2.2 and 2.3). Then the pore pressure

477 and shear stress are computed at the interface $y \rightarrow 0^\pm$, which finally grants expressions
478 presented in Section 3.1.

479 References

- 480 [1] I. Svetlizky, J. Fineberg, Classical shear cracks drive the onset of dry frictional motion, *Nature*
481 509 (7499) (2014) 205. doi:10.1038/nature13202.
- 482 [2] C. Marone, Laboratory-derived friction laws and their application to seismic faulting, *Annu. Rev. Earth*
483 *Pl. Sc.* 26 (1) (1998) 643–696.
- 484 [3] Z. Peng, J. Gombert, An integrated perspective of the continuum between earthquakes and slow-slip
485 phenomena, *Nat. Geosci.* 3 (9) (2010) 599. doi:10.1038/ngeo940.
- 486 [4] G. C. Beroza, S. Ide, Slow earthquakes and nonvolcanic tremor, *Annu. Rev. Earth Pl. Sc.* 39 (1) (2011)
487 271–296. doi:10.1146/annurev-earth-040809-152531.
- 488 [5] M. D. Zoback, A. Kohli, I. Das, M. W. McClure, The importance of slow slip on faults during hydraulic
489 fracturing stimulation of shale gas reservoirs, in: *SPE Americas Unconventional Resources Conference*,
490 *Society of Petroleum Engineers*, 2012.
- 491 [6] Y. Guglielmi, F. Cappa, J.-P. Avouac, P. Henry, D. Elsworth, Seismicity triggered by fluid injection–
492 induced aseismic slip, *Science* 348 (6240) (2015) 1224–1226. doi:10.1126/science.aab0476.
- 493 [7] J. Galeano, P. Espanol, M. Rubio, Experimental and theoretical results of stress relaxations in a model
494 of earthquake dynamics, *Europhys. Lett.* 49 (4) (2000) 410.
- 495 [8] M. A. Rubio, J. Galeano, Stick-slip dynamics in the relaxation of stresses in a continuous elastic
496 medium, *Phys. Rev. E* 50 (2) (1994) 1000.
- 497 [9] T. Baumberger, C. Caroli, O. Ronsin, Self-healing slip pulses along a gel/glass interface, *Phys. rev.*
498 *lett.* 88 (7) (2002) 075509.
- 499 [10] T. Baumberger, C. Caroli, O. Ronsin, Self-healing slip pulses and the friction of gelatin gels, *Eur. Phys.*
500 *J. E* 11 (1) (2003) 85–93.
- 501 [11] O. Ronsin, T. Baumberger, C. Hui, Nucleation and propagation of quasi-static interfacial slip pulses,
502 *J. Adhesion* 87 (5) (2011) 504–529.
- 503 [12] N. Kato, A possible model for large preseismic slip on a deeper extension of a seismic rupture plane,
504 *Earth Planet. Sc. Lett.* 216 (1-2) (2003) 17–25.
- 505 [13] A. M. Rubin, Episodic slow slip events and rate-and-state friction, *J. Geophys. Res. Solid Earth*
506 113 (B11). doi:10.1029/2008JB005642.
- 507 [14] P. Segall, A. M. Rubin, A. M. Bradley, J. R. Rice, Dilatant strengthening as a mechanism for slow slip
508 events, *J. Geophys. Res. Solid Earth* 115 (B12).

- 509 [15] Y. Bar-Sinai, E. A. Brener, E. Bouchbinder, Slow rupture of frictional interfaces, *Geophys. Res. Lett.*
510 39 (3). doi:10.1029/2011GL050554.
- 511 [16] Y. Bar-Sinai, R. Spatschek, E. A. Brener, E. Bouchbinder, On the velocity-strengthening behavior of
512 dry friction, *J. Geophys. Res. Solid Earth* 119 (3) (2014) 1738–1748. doi:10.1002/2013JB010586.
- 513 [17] A. H. Kohli, M. D. Zoback, Frictional properties of shale reservoir rocks, *J. Geophys. Res. Solid Earth*
514 118 (9) (2013) 5109–5125. doi:10.1002/jgrb.50346.
- 515 [18] M. J. Ikari, C. Marone, D. M. Saffer, A. J. Kopf, Slip weakening as a mechanism for slow earthquakes,
516 *Nat. Geosci.* 6 (6) (2013) 468. doi:10.1038/ngeo1818.
- 517 [19] D. M. Saffer, L. M. Wallace, The frictional, hydrologic, metamorphic and thermal habitat of shallow
518 slow earthquakes, *Nat. Geosci.* 8 (8) (2015) 594. doi:10.1038/ngeo2490.
- 519 [20] R. Bürgmann, The geophysics, geology and mechanics of slow fault slip, *Earth Planet. Sc. Lett.* 495
520 (2018) 112–134.
- 521 [21] J. R. Rice, D. A. Simons, The stabilization of spreading shear faults by coupled deformation-
522 diffusion effects in fluid-infiltrated porous materials, *J. Geophys. Res.* 81 (29) (1976) 5322–5334.
523 doi:10.1029/JB081i029p05322.
- 524 [22] J. R. Rice, M. P. Cleary, Some basic stress diffusion solutions for fluid-saturated elastic porous media
525 with compressible constituents, *Rev. Geophys.* 14 (2) (1976) 227–241. doi:10.1029/RG014i002p00227.
- 526 [23] J. W. Rudnicki, D. A. Koutsibelas, Steady propagation of plane strain shear cracks on an impermeable
527 plane in an elastic diffusive solid, *Int. J. Solids Struct.* 27 (2) (1991) 205–225.
- 528 [24] J. Weertman, Unstable slippage across a fault that separates elastic media of different elastic constants,
529 *J. Geophys. Res. Solid Earth* 85 (B3) (1980) 1455–1461.
- 530 [25] F. M. Chester, J. P. Evans, R. L. Biegel, Internal structure and weakening mechanisms of the san
531 andreas fault, *J. Geophys. Res.* 98 (B1) (1993) 771–786.
- 532 [26] J. S. Caine, J. P. Evans, C. B. Forster, Fault zone architecture and permeability structure, *Geology*
533 24 (11) (1996) 1025–1028.
- 534 [27] C. A. Wibberley, T. Shimamoto, Internal structure and permeability of major strike-slip fault zones:
535 the Median Tectonic Line in Mie Prefecture, Southwest Japan, *J. Struct. Geol.* 25 (1) (2003) 59–78.
- 536 [28] J. Behnsen, D. Faulkner, Water and argon permeability of phyllosilicate powders under medium to
537 high pressure, *Earth Planet. Sc. Lett.* 116 (B12).
- 538 [29] F. Chester, J. M. Logan, Implications for mechanical properties of brittle faults from observations of
539 the punchbowl fault zone, california, *Pure Appl. Geophys.* 124 (1-2) (1986) 79–106.
- 540 [30] T. Mitchell, D. Faulkner, Towards quantifying the matrix permeability of fault damage zones in low
541 porosity rocks, *Earth Planet. Sc. Lett.* 339 (2012) 24–31.
- 542 [31] F. M. Chester, J. S. Chester, Ultracataclasite structure and friction processes of the punchbowl

- 543 fault, San Andreas system, California, *Tectonophysics* 295 (1) (1998) 199 – 221. doi:10.1016/S0040-
544 1951(98)00121-8.
- 545 [32] F. M. Chester, J. S. Chester, D. L. Kirschner, S. E. Schulz, J. P. Evans, Structure of large-displacement,
546 strike-slip fault zones in the brittle continental crust, *Rheology and deformation in the lithosphere at*
547 *continental margins* 1 (2004) 223–260.
- 548 [33] O. Dor, T. K. Rockwell, Y. Ben-Zion, Geological observations of damage asymmetry in the structure of
549 the San Jacinto, San Andreas and Punchbowl faults in Southern California: A possible indicator for pre-
550 ferred rupture propagation direction, *Pure Appl. Geophys.* 163 (2) (2006) 301–349. doi:10.1007/s00024-
551 005-0023-9.
- 552 [34] J. W. Rudnicki, J. R. Rice, Effective normal stress alteration due to pore pressure changes induced
553 by dynamic slip propagation on a plane between dissimilar materials, *J. Geophys. Res. Solid Earth*
554 111 (B10). doi:10.1029/2006JB004396.
- 555 [35] E. M. Dunham, J. R. Rice, Earthquake slip between dissimilar poroelastic materials, *J. Geophys. Res.*
556 *Solid Earth* 113 (B9), b09304. doi:10.1029/2007JB005405.
- 557 [36] J. R. Rice, N. Lapusta, K. Ranjith, Rate and state dependent friction and the stability of sliding
558 between elastically deformable solids, *J. Mech. Phys. Solids* 49 (9) (2001) 1865–1898.
- 559 [37] E. A. Brener, M. Weikamp, R. Spatschek, Y. Bar-Sinai, E. Bouchbinder, Dynamic instabilities of
560 frictional sliding at a bimaterial interface, *J. Mech. Phys. Solids* 89 (2016) 149–173.
- 561 [38] M. Aldam, S. Xu, E. A. Brener, Y. Ben-Zion, E. Bouchbinder, Nonmonotonicity of the frictional
562 bimaterial effect, *J. Geophys. Res. Solid Earth* 122 (10) (2017) 8270–8284.
- 563 [39] H. Shlomag, J. Fineberg, The structure of slip-pulses and supershear ruptures driving slip in bimaterial
564 friction, *Nat. Commun.* 7 (2016) 11787.
- 565 [40] Y. Song, J. W. Rudnicki, Plane-strain shear dislocation on a leaky plane in a poroelastic solid, *J. Appl.*
566 *Mech.* 84 (2) (2017) 021008.
- 567 [41] M. F. Linker, J. H. Dieterich, Effects of variable normal stress on rock friction: Observations and
568 constitutive equations, *J. Geophys. Res. Solid Earth* 97 (B4) (1992) 4923–4940. doi:10.1029/92JB00017.
- 569 [42] E. Detournay, A. H.-D. Cheng, Fundamentals of poroelasticity, in: *Analysis and Design Methods*,
570 Elsevier, 1995, pp. 113–171.
- 571 [43] M. Svärd, J. Nordström, Review of summation-by-parts-operators schemes for initial-boundary-value
572 problems, *J. Comput. Phys.* 268 (0) (2014) 17–38.
- 573 [44] D. C. Del Rey Fernández, J. E. Hicken, D. W. Zingg, Review of summation-by-parts operators with
574 simultaneous approximation terms for the numerical solution of partial differential equations, *Comput.*
575 *Fluids* 95 (2014) 171 – 196.
- 576 [45] M. H. Carpenter, D. Gottlieb, S. Abarbanel, Time-stable boundary conditions for finite-difference

- 577 schemes solving hyperbolic systems: Methodology and application to high-order compact schemes, *J.*
578 *Comput. Phys.* 111(2) (1994) 220–236.
- 579 [46] K. Torberntsson, V. Stiernström, K. Mattsson, E. M. Dunham, A finite difference method for earth-
580 quake sequences in poroelastic solids, *Computat. Geosci.* 22 (5) (2018) 1351–1370. doi:10.1007/s10596-
581 018-9757-1.
- 582 [47] H. Gao, D. A. Schmidt, R. J. Weldon, Scaling relationships of source parameters for slow slip events,
583 *Bull. Seismol. Soc. Am* 102 (1) (2012) 352–360.
- 584 [48] A. Ghosh, J. E. Vidale, J. R. Sweet, K. C. Creager, A. G. Wech, H. Houston, E. E. Brodsky, Rapid,
585 continuous streaking of tremor in Cascadia, *Geochem. Geophys. Geosy.* 11 (12).
- 586 [49] Y. Peng, A. M. Rubin, High-resolution images of tremor migrations beneath the Olympic penin-
587 sula from stacked array of arrays seismic data, *Geochem. Geophys. Geosy.* 17 (2) (2016) 587–601.
588 doi:10.1002/2015GC006141.
- 589 [50] W. B. Frank, B. Rousset, C. Lasserre, M. Campillo, Revealing the cluster of slow transients behind a
590 large slow slip event, *Sci. Adv.* 4 (5). doi:10.1126/sciadv.aat0661.
- 591 [51] D. R. Shelly, G. C. Beroza, S. Ide, Complex evolution of transient slip derived from precise tremor
592 locations in western shikoku, japan, *Geochem. Geophys. Geosy.* 8 (10). doi:10.1029/2007GC001640.
- 593 [52] D. R. Shelly, Migrating tremors illuminate complex deformation beneath the seismogenic san andreas
594 fault, *Nature* 463 (7281) (2010) 648.
- 595 [53] R. Nakata, N. Suda, H. Tsuruoka, Non-volcanic tremor resulting from the combined effect of Earth
596 tides and slow slip events, *Nat, Geosci.* 1 (10) (2008) 676.
- 597 [54] D. A. Wiens, S. Anandkrishnan, J. P. Winberry, M. A. King, Simultaneous teleseismic and geodetic
598 observations of the stick–slip motion of an Antarctic ice stream, *Nature* 453 (7196) (2008) 770.
- 599 [55] N. R. Iverson, Shear resistance and continuity of subglacial till: hydrology rules, *J. Glaciol.* 56 (200)
600 (2010) 1104–1114.
- 601 [56] W. H. Schulz, J. P. McKenna, J. D. Kibler, G. Biavati, Relations between hydrology and velocity
602 of a continuously moving landslide-Evidence of pore-pressure feedback regulating landslide motion?,
603 *Landslides* 6 (3) (2009) 181–190.
- 604 [57] A. Verruijt, Displacement functions in the theory of consolidation or in thermoelasticity, *Zeitschrift für*
605 *angewandte Mathematik und Physik ZAMP* 22 (5) (1971) 891–898.
- 606 [58] J. McNamee, R. E. Gibson, Plane strain and axially symmetric problems of the consolidation of a
607 semi-infinite clay stratum, *Q. J. Mech. Appl. Math.* 13 (2) (1960) 210–227.
- 608 [59] M. A. Biot, General solutions of the equations of elasticity and consolidation for a porous material, *J.*
609 *Appl. Mech.* 23 (1) (1956) 91–96.